

# A methodology to aid in the design of naval steels: Linking first principles calculations to mesoscale modeling

G. Spanos<sup>a,\*</sup>, A.B. Geltmacher<sup>a</sup>, A.C. Lewis<sup>a</sup>, J.F. Bingert<sup>c</sup>, M. Mehl<sup>b</sup>,  
D. Papaconstantopoulos<sup>b</sup>, Y. Mishin<sup>d</sup>, A. Gupta<sup>a,e</sup>, P. Matic<sup>a</sup>

<sup>a</sup> Naval Research Laboratory, Multifunctional Materials Branch, Code 6350, Washington, DC 20375, United States

<sup>b</sup> Naval Research Laboratory, Center for Computational Materials Science, Code 6390, Washington, DC 20375, United States

<sup>c</sup> Los Alamos National Laboratory, MST-8, Los Alamos, NM 87545, United States

<sup>d</sup> George Mason University, Department of Physics and Astronomy, Fairfax, VA 22030-4444, United States

<sup>e</sup> GeoCenters Inc., Fort Washington, MD 20749, United States

Received 14 April 2006; received in revised form 19 October 2006; accepted 24 October 2006

## Abstract

This paper provides a brief overview of a multidisciplinary effort at the Naval Research Laboratory aimed at developing a computationally-based methodology to assist in the design of advanced Naval steels. This program uses multiple computational techniques ranging from the atomistic length scale to continuum response. First-principles electronic structure calculations using density functional theory were employed, semi-empirical angular dependent potentials were developed based on the embedded atom method, and these potentials were used as input into Monte-Carlo and molecular dynamics simulations. Experimental techniques have also been applied to a super-austenitic stainless steel (AL6XN) to provide experimental input, guidance, verification, and enhancements to the models. These experimental methods include optical microscopy, scanning electron microscopy, transmission electron microscopy, electron backscatter diffraction, and serial sectioning in conjunction with computer-based three-dimensional reconstruction and quantitative analyses. The experimental results are also used as critical input into mesoscale finite element models of materials response.

© 2006 Elsevier B.V. All rights reserved.

**Keywords:** Materials design; Atomistic modeling; Embedded atom method (EAM); Three-dimensional (3D) analysis; Finite element modeling (FEM); Austenitic stainless steels

## 1. Introduction

Alloy steels will continue to be a major structural material in both existing and new US Navy ships and submarines in the foreseeable future, due to their relatively low cost, good combination of mechanical properties, and the existing infrastructure for their processing and fabrication. Hence, it is beneficial for the US Navy to build a naval steels development program which would help to enable design engineers to specify materials performance criteria for a specific Naval structure, while simultaneously determining enhanced/optimized alloy compositions and processing procedures, all in a reasonable timeframe. Performance optimization criteria of interest include (but are not limited to) improving corrosion resistance, maximizing mate-

rial strength and toughness, reducing magnetic signature, and minimizing costs. Currently, most conventional material development methodologies require many years, due to their reliance on time-consuming empirical approaches to alloy and process design. A “Steels-by-Design” program must therefore include state-of-the-art computational techniques as well as limited, but judicious, experiments, in order to reduce the time of development and implementation of new structural alloys. In particular, such a program should include computational techniques which span across not only multiple scientific disciplines, but also across various length scales, ranging from the atomic level (Å), to the mesoscale (μm), to the macroscale (mm and greater). These models need to be performed in conjunction with critical experiments that provide for quantitative input, guidance, verification, and enhancements to the models.

The “Materials-by-Design” concept is not a new one, and has been brought to prominence within the last decade or so in large part due to the efforts of Olson and coworkers at Northwestern

\* Corresponding author. Tel.: +1 202 767 5799; fax: +1 202 767 2623.  
E-mail address: [george.spanos@nrl.navy.mil](mailto:george.spanos@nrl.navy.mil) (G. Spanos).

University (e.g., see [1–3]). They have combined thermodynamics, kinetics modeling, first principles calculations, and materials properties analysis in a quantitative fashion, with the ultimate goal of providing alloy compositions and processing cycles for specific applications. A central theme of their approach has been to consider the required final materials properties at the earliest stages in the design cycle. In many ways their approach has served as a template for most other materials by design programs (e.g., [4]), including the present one.

One of the “Grand Challenges” identified by the US Office of Naval Research in the late 1990s was the need to invest more strongly in such a Materials-by-Design approach for the development of advanced Naval materials, particularly alloy steels. To this end, a team of researchers from several sub-disciplines at the Naval Research Laboratory (NRL), along with scientists from George Mason University and Los Alamos National Laboratory, was assembled to develop the framework for such a program. This team includes the physicists, computational materials scientists, experimental materials scientists, and mechanical engineers who comprise the author list of this paper. The areas of expertise employed include first principles methods, semi-empirical atomistic calculations, a variety of microstructural characterization techniques, and mesoscale modeling of material response (stress/strain evolution).

One of the primary overall goals of the program described here is to develop a methodology at NRL for helping to reduce the development time of future Navy steels. In some respects, this program compliments the well established efforts of Olson and coworkers [1,2], while at the same time focuses on other types of alloy systems, and brings to bear some different, new tools (e.g., new 3D analysis capabilities, advanced atomistic and tight-binding calculations, etc.). In addition to developing alloys with a good combination of strength and toughness, two required performance criteria of immediate importance include eliminating (or significantly reducing) magnetic signature and improving corrosion resistance, in order to enhance performance capabilities and reduce total ownership costs of future Naval structures. Along these lines, a commercial superaustenitic stainless steel developed by Allegheny Ludlum (designated “AL6XN”) was selected as a baseline composition from which to begin the experimental portion of this program, in order to provide quantitative input, guidance, verification, and enhancements to the models. The composition of this alloy is provided in Table 1.

An important aspect of this research is thus the use of multiple computational techniques ranging from the atomistic

length scale to the continuum response of a material. This includes employing first-principles electronic structure calculations to create a database of energetic and electronic structure information for a variety of crystal structures. This database was also used to create a parameterized tight-binding (TB) Hamiltonian which can be used to study larger systems, at a computational cost low enough to permit molecular dynamics calculations. Semi-empirical angular dependent potentials (ADPs) were developed based on the embedded atom method (EAM), and were fitted to the first principles database as well as to existing experimental data. These potentials were then used in Monte-Carlo and molecular dynamics simulations, which were employed to calculate grain boundary structure, energy, and segregation. Examples of output calculated by these techniques include formation energies of phases, elastic constants, coefficients of thermal expansion, and grain boundary structure, energy, and segregation behavior. Experimental techniques employed include optical microscopy, scanning electron microscopy (SEM), transmission electron microscopy (TEM), energy dispersive spectroscopy (EDS), electron backscatter diffraction (EBSD) analysis with orientation mapping (OM), and serial sectioning in conjunction with computer-based three-dimensional (3D) reconstruction, scientific visualization, and quantitative analyses. Results thus obtained include misorientation and 3D boundary plane analyses, compositional analyses of precipitates and grain boundaries, and 3D morphology, interconnectivity, and crystallography of matrix and precipitate grains. These experiments guide the lower-scale first principles and atomistic models, and are also required for image-based mesoscale finite element models (FEMs) of materials response which use real (experimentally obtained) 2D and 3D images/micrographs of microstructures as input. In such modeling, particular emphasis is placed on identification of critical microstructural features that generate local regions of high stress and strain that will initiate localized plastic deformation and potentially failure in the material. In all components of this program, the results are integrated by passing data (in both directions) between team members and across various length scales.

The purpose of the present paper is thus to provide a brief overview of our methodology and team, to present a few representative examples of results obtained to date, and to demonstrate how such results fit together across the various sub-disciplines and length scales. Since a comprehensive report of all of the results produced from the current effort would be too lengthy to present in this single paper, further specifics and more detailed results are provided in a number of companion papers to this one [5–8]. Additionally, ongoing efforts are centered about further application of this methodology to alloy design.

## 2. Computational and experimental methodology

A suite of computational tools employed previously by the various members of the team assembled here has been further developed and integrated over a range of length scales, along with relevant experimental characterization capabilities for model development and verification. These computational tools allow for data to be passed from the smallest to rela-

Table 1  
Composition of AL6XN<sup>®</sup> Alloy (Allegheny Ludlum)

Element	wt. %
Fe	48.2
Ni	24
Cr	20.5
Mo	6.3
Si	0.4
Mn	0.4
N	0.22
C	0.02

tively large length scales, providing for enhanced modeling, and ensuring consistency in the material property and performance calculations. Examples of the types of data that are passed (in both directions) between tasks and across length scales include: formation energies of phases, interatomic potentials, elastic constants, coefficients of thermal expansion, grain boundary structure and segregation, grain boundary statistics (including frequency of special grain boundaries), three-dimensional morphology and interconnectivity of matrix and precipitate grains, grain crystallography/texture, local stress and strain states, and yield surfaces. Before presenting some of the results of the calculations and experiments, the various techniques and models employed will be described in more detail.

### 2.1. First principles and atomistic models

“First principles” refers to calculations that are based on quantum mechanics and require no experimental input. These types of techniques are computationally intensive and are thus usually limited to small numbers (hundreds) of atoms. The first principles models employed here make use of density functional theory (DFT) [9] as applied in the linear augmented plane wave (LAPW) [10] method using the generalized gradient approximation (GGA) [11]. These models have been employed to calculate (among other properties) the energy of formation, and thus the relative stability, of a number of possible relevant phases. They are also used in conjunction with more empirical formulations to develop atomistic potentials which can be used in less computationally intensive types of simulations (see below). In parallel with the first principles calculations, the Stoner criterion [12] was occasionally employed to approximate magnetic behavior. Specifically, the product of the density of states at the Fermi level,  $N(E_F)$ , times a matrix element  $\langle I \rangle$ , is known as the Stoner criterion, and a material is predicted to be ferromagnetic if this product is greater than 1.0. The parameter  $\langle I \rangle$  is determined from first-principles from the angular momentum components of  $N(E_F)$  and the radial wave functions as computed in a band structure calculation. The parameter  $\langle I \rangle$  is related to the magnetic susceptibility,  $S$ , through the expression:  $S = 1/(1 - N(E_F)\langle I \rangle)$ .

Data derived from the first-principles calculations can be used to create Hamiltonians which can be extended to significantly larger systems, i.e. thousands of atoms with quantum mechanics, and millions of atoms with atomistic potentials. In the present case, the tight-binding method (TBM) [13] has been employed to develop the Hamiltonians by fitting to first principles results. Interatomic potentials have been constructed by employing the angular-dependent potentials (ADP) method with parameters fit to a combination of the first principles (LAPW) calculations, TBM calculations, and experimental information.

In particular, a new ADP method, which is a generalization of the embedded atom method (EAM) has been developed to address the strong need for non-central force potentials for transition metals. This method can include explicit temperature dependence of interatomic forces as well as magnetic effects [6], which allows for significant improvements in the accuracy and utility of the models. More specifically, this technique begins to overcome limitations of previous EAM models of Fe in prop-

erly accounting for the FCC-to-BCC transition in steels. The new ADP potential for Fe and the Fe–Ni binary system is employed in conjunction with Monte-Carlo simulations to calculate grain boundary structure and segregation. The virtual “mechanical testing” of grain boundary decohesion [14] can then also be performed to assess the effect of the segregation on mechanical strength of grain boundaries.

In all cases, relevant parameters are passed between the various models, and the models are being continuously guided, verified, and enhanced by critical experimental input, in order to insure that they address realistic material characteristics and properties of importance in developing new alloy steels. Details of how the experimental data are integrated with the computational models will become evident in Sections 2.2, 2.3 and 3.

### 2.2. Microstructural characterization

A variety of microscopy techniques are being employed in order to provide the experimental input that is so critical to verification and guidance of the models, and thus ultimately to the predictive efforts of this program. These techniques, which have been initially applied to the baseline AL6XN alloy, include conventional optical microscopy, scanning electron microscopy (SEM), transmission electron microscopy (TEM), and energy dispersive spectroscopy (EDS). These methods are used to determine the morphology, interconnectivity, crystallography, and local elemental chemistry of the matrix (austenite) and precipitate (sigma) phases. Additionally, electron backscatter diffraction (EBSD) analysis in conjunction with orientation mapping (OM) is employed to obtain crystallographic grain orientations and grain boundary misorientations and types, over a statistically relevant number of grains (i.e., hundreds of grains for each map).

The aforementioned experimental techniques are all based on observation of two-dimensional (2D) planes of polish, or nearly 2D slices through the material in the case of a TEM thin foil. As has now been shown by a number of different studies in a variety of materials systems, these conventional 2D techniques are simply inadequate for accurate determination of the true 3D nature of the microstructure for most materials of even moderate microstructural complexity (e.g., see [15–22]). Thus, serial sectioning with computer-based three-dimensional (3D) reconstruction, scientific visualization, and quantitative analysis have been employed in conjunction with optical microscopy, SEM, and EBSD/OM to provide critical 3D information on the morphology, interconnectivity, and crystallography of the austenite and sigma phases in the superaustenitic stainless steel employed here (AL6XN). In addition to providing guidance and verification for the atomistic models, this 3D data also serves as required input for the 3D image-based mesoscale FEM models used to predict materials response.

### 2.3. Mesoscale modeling of material response

In employing computational techniques to aid in alloy design, the atomistic models described above can be used to predict

some of the key microstructural features (e.g., phase stability, grain boundary structure and segregation, etc.) and important properties (e.g., magnetic behavior, elastic properties, etc.), as a function of alloy chemistry and thermomechanical processing. But modeling of larger scale materials response is also required to develop predictive capability which will enable criteria such as yield strength and/or impact toughness to be implemented in the alloy design cycle. In this regard, it is important to be able to predict the evolution of stress and strain generated in real microstructures, to levels which ultimately result in the initiation of macroscopic yield and eventually failure.

Image-based mesoscale modeling techniques developed at NRL [8,23] have therefore been employed. The models are termed “image-based” because the finite element mesh geometries are derived from micrographs taken from real microstructures (experimentally obtained), rather than from some assumed or simulated grain distributions or structures. Additionally, the crystallographic orientation of each grain in the models is assigned based on the experimental measurements, rather than on a statistically representative distribution of orientations. These models are thus initially derived directly from 2D orientation maps (measured using EBSD), which give the local grain orientation, phase type, and presence or absence of a grain boundary, at each pixel in the 2D mesh. Finite element analyses of stress/strain evolution are therefore performed in which fundamental types of displacement boundary conditions are applied using ABAQUS<sup>TM</sup> software, to meshes developed from the experimental data.

Additionally, similar to the 2D models, 3D image-based mesoscale models are employed which use as input the experimental 3D reconstructions of the microstructure. In these models, a 3D reconstructed volume is converted into a finite element mesh as a regular grid with elements centered around each voxel [8]. A single averaged crystallographic orientation is assigned to each grain in the 3D mesh. As in the 2D simulations, different simple displacement boundary conditions are then applied, and stress and strain are allowed to evolve within the microstructure. Particular emphasis is placed on identification of local regions of maximum stress and strain states which indicate potential microstructural features where plastic yield, strain localization, and/or initiation of damage or even failure will occur.

From the finite element data, stress and strain state visualization techniques have also been developed, in which the principle stresses and strains are mapped in the appropriate stress or strain space to visualize the stress/strain states of all locations in the specimen geometry employed in the model. The major regions of these plots represent states of uniaxial tension, uniaxial compression, pure shear, and equal biaxial tension.

### 3. Results and discussion

In order to provide some detail of the types of output resulting from this approach, a few representative results from each component of the program will now be presented. Further detailed results are reported in a number of other related references [5–8,24].

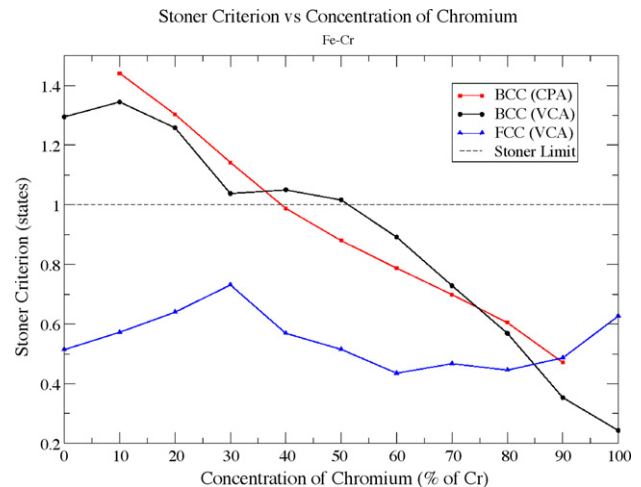


Fig. 1. Stoner criterion for magnetic stability in the Fe–Cr system (CPA: coherent potential approximation; VCA: virtual crystal approximation).

#### 3.1. First principles/atomistic model results

Initially, the Stoner criterion [12] was used as an approximation to determine the feasibility of significantly reducing the magnetic signature of advanced alloy steels in the BCC (body centered cubic) state. The results indicated that this cannot be realistically accomplished in BCC ferrous alloys of interest. For instance, for the particular case of Cr in Fe, in order to reduce the Stoner parameter to less than 1 (an empirical threshold often used to represent a minimum magnetic signature), these calculations indicate that unrealistically large amounts (~40% or more) of Cr would be required—see Fig. 1. At these levels of Cr, both thermodynamic calculations and experimental observations indicate that the BCC structure would be unstable at room temperature.

DFT/LAPW calculations were also performed to determine the stability of different possible phases in the Fe–Ni system. These results, shown in Fig. 2, indicate that FCC-based phases, including the tetragonal  $L_{10}$  and  $L_{12}$  phases, are lowest in energy. In more recent calculations, both Cr and C are being considered, in addition to Ni. A major objective of these calculations is to identify any “new” phases that might either offer

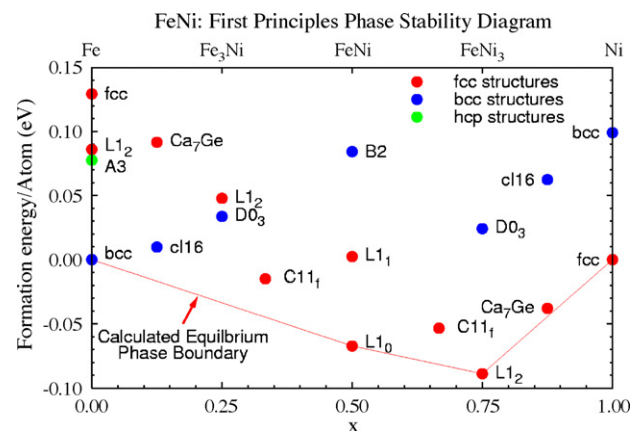


Fig. 2. Calculated Fe–Ni phase stability diagram.



benefits, or be deleterious, to material properties, in order to include them into design cycle considerations. One such example is the possibility of formation of an  $\text{Fe}_2\text{Ni}$  phase in what is termed the  $\text{C11}_f$ -structure. This structure consists of two layers of iron with one layer of nickel, stacked in the  $[001]$  direction. The first principles calculations performed here indicate that this structure can have a very low energy (see Fig. 2), but this phase has not been widely reported in the alloys currently under consideration. If this layered compound phase formed in certain distributions, it might, for instance, contribute to strengthening. As just one example of how information from the first principles calculations is then passed on to the experimental characterization team members, transmission electron microscopy (TEM) is being performed in the base alloy, AL6XN, in part to verify the presence or absence of the  $\text{C11}_f$ - $\text{Fe}_2\text{Ni}$  phase. Initial TEM studies have not revealed any  $\text{Fe}_2\text{Ni}$  phase.

One test of the accuracy and/or utility of the tight-binding semi-empirical atomistic potentials and the LAPW calculations is to compare the formation energies and/or elastic constants of specific phases calculated by each of these methods to experiments. In this regard, Table 2 shows a comparison of elastic constants for the magnetic elements, Fe, Co, and Ni, computed using the tight-binding and/or the LAPW method, and the corresponding experimental values. The tight-binding method was also used to calculate vacancy formation energies,  $E_{\text{vf}}$ , using a 216-atom super cell, including relaxation. For Fe the calculated  $E_{\text{vf}}$  is 2.33 eV compared to the experimental value of 2.0 eV. The Ni calculation turned out to be even more accurate, matching almost exactly the experimental value of 1.6 eV.

Additionally, for the many different types of calculations employed in this project, more recent efforts have been focused on including simultaneously the contributions of the major alloying elements of interest for the alloy steels under consideration, i.e., Fe, Ni, Cr and C. The interatomic potentials developed in this program have been used in Monte-Carlo simulations of grain boundary structure and segregation, with particular emphasis placed on the types of grain boundaries that the experimental input (see Section 3.2) suggests are of most importance. In this vein, segregation of Cr and Ni to grain boundaries is of practical importance in that it can dramatically affect corrosion and other properties at and adjacent to the grain boundaries. Initial calculations have shown that for the same lattice misorientation across a grain boundary (i.e., FCC  $\Sigma 9$  boundaries in Fe–Ni alloys), the segregation of Ni depends not only on the misorientation between the grains, but is strongly affected by

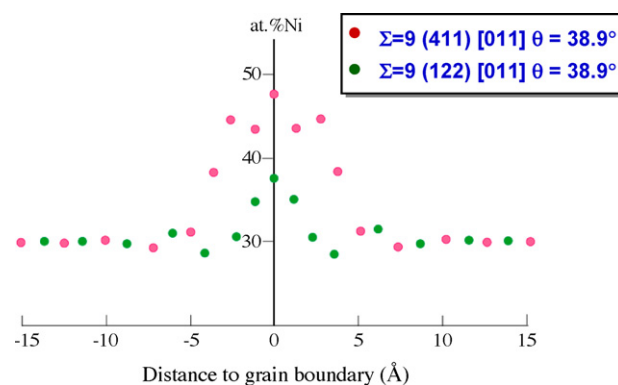


Fig. 3. Ni segregation at two  $\Sigma 9$  boundaries in FCC Fe–30 at.% Ni alloys (austenite) at  $T = 1200$  K; each of these  $\Sigma 9$  boundaries has a different plane inclination. This result demonstrates that the segregation depends sensitively on the boundary plane inclination.

changes in the 3D inclination of the boundary—see Fig. 3. This difference in segregation behavior is obviously due to changes in boundary structure that result from different boundary inclinations, in similar fashion to results reported for segregation to different boundary structures in BCC  $\alpha$ -iron [25]. In particular, Fig. 3 shows the calculated Ni concentration versus distance from the grain boundary for two  $\Sigma 9$  boundaries (as defined by coincidence-site lattice nomenclature) with the same grain boundary misorientation but different crystallographic normals. As seen in the figure, significant differences in the Ni concentration, as well as the distance over which fluctuations in concentration occur, are observed for the two boundary types. Conventional EBSD can measure the crystallography and misorientation between two grains (i.e. four of the five degrees of freedom needed to define the boundary fully), however, the inclination can only be measured using 3D sectioning and reconstruction techniques. The differences in segregation caused by 3D boundary structure shown through the calculations described here, and the anticipated corresponding effects on corrosion resistance are significant, and further indicate that 3D microstructural analysis is required for a complete understanding of the behavior of this material.

The grain boundary segregation characteristics, as well the boundary structures (see examples in Fig. 4) and energies provide important information for predictions of material response, since these parameters affect such properties as slip across the boundaries, decohesion of boundaries during failure, and predictive models of grain growth.

Table 2  
Elastic constants calculated for Fe, Ni, Co

$a = a_{\text{exp}}$	Fe			Ni		Co <sup>+</sup>		
	TB	LAPW	Experimental	Experimental	TB	TB	LAPW	Experimental
B	138	159	173	185	175	$\text{C}_{11}$	306	325
$\text{C}_{11}-\text{C}_{12}$	128	112	96	95	114	$\text{C}_{12}$	231	165
$\text{C}_{11}$	223	234	237	249	251	$\text{C}_{13}$	222	105
$\text{C}_{12}$	95	121	141	153	137	$\text{C}_{33}$	283	365
$\text{C}_{44}$	78	83	116	118	69	$\text{C}_{44}$	36	90
								66

$\text{C}_{11}-\text{C}_{12}$  and  $\text{C}_{44}$  are not included in the fits.

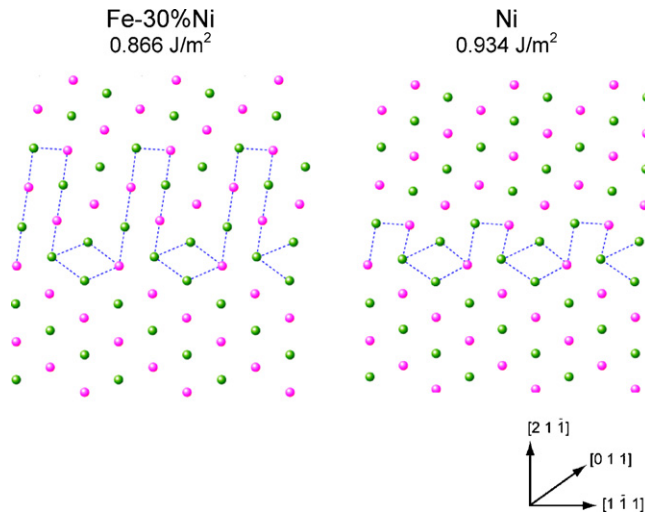


Fig. 4. Calculated atomic structures and energies for the  $\Sigma 3(211)[011]$  boundary in the Fe–30% Ni alloy (austenite) and in pure Ni. The lines outline the rhombic structural units forming the boundary structure and the intrinsic stacking fault ribbons extending from the boundary into the upper grain. Each stacking fault terminates at a Shockley partial dislocation. The longer stacking faults in the austenite point to the smaller stacking fault energy, in comparison with pure Ni. This simulation demonstrates the significant effect of chemical composition on grain boundary structure.

### 3.2. Microstructural characterization

Electron backscatter diffraction (EBSD) and the associated orientation mapping (OM) in 2D were utilized to provide statistics on austenite grain orientations and grain boundary types. A typical orientation map (also referred to as an “Inverse Pole Figure Map”) is shown in Fig. 5(a), and a “boundary type” map from a representative area of the austenite matrix is pre-

sented in Fig. 5(b). These results provide input to the alloy design approach in a number of ways. For example,  $\Sigma 3$  boundaries are quantified and shown to be very prominent in this recrystallized FCC material (Fig. 5(b)), and these boundaries have been reported to significantly affect corrosion resistance as well as mechanical behavior [26–33]. In particular,  $\Sigma 3$  boundaries are expected to enhance corrosion resistance [26] but may degrade fatigue properties [27]. Additionally, these orientation maps provide critical guidance to the first principles calculations and atomistic models by defining the boundary types (and their relative frequency) that are present in the steel, and that are thus emphasized in the calculations (such as  $\Sigma 3$  and  $\Sigma 9$  boundaries—compare Figs. 3–5). This information then provides the initial conditions for the atomistic calculations of grain boundary structure, energy, and segregation (e.g., see Figs. 3 and 4). Finally, microstructural data such as that shown in Fig. 5(a) is used as direct input to the mesoscale image-based models of materials response (see Section 3.3).

Analyses of precipitate phases, particularly sigma in the AL6XN, are also performed using a combination of optical microscopy, OM/EBSD, and TEM. Sigma is a non-stoichiometric secondary intermetallic phase typically consisting of  $(\text{Fe, Ni})_x(\text{Cr, Mo})_y$  in austenitic steels, and it can be especially deleterious to fracture toughness. Fig. 6 shows sigma precipitates along the AL6XN plate centerline, both at austenite grain boundaries and within austenite grains. Further analyses have shown that the sigma particles on the grain boundaries contribute to pinning of these boundaries during recrystallization [7]. Since these particles can have a detrimental effect on both mechanical performance and corrosion properties, their volume fraction, morphology, connectivity, crystallography, and chemical composition must be properly determined, and considered in the modeling efforts, in order to elucidate their potential for

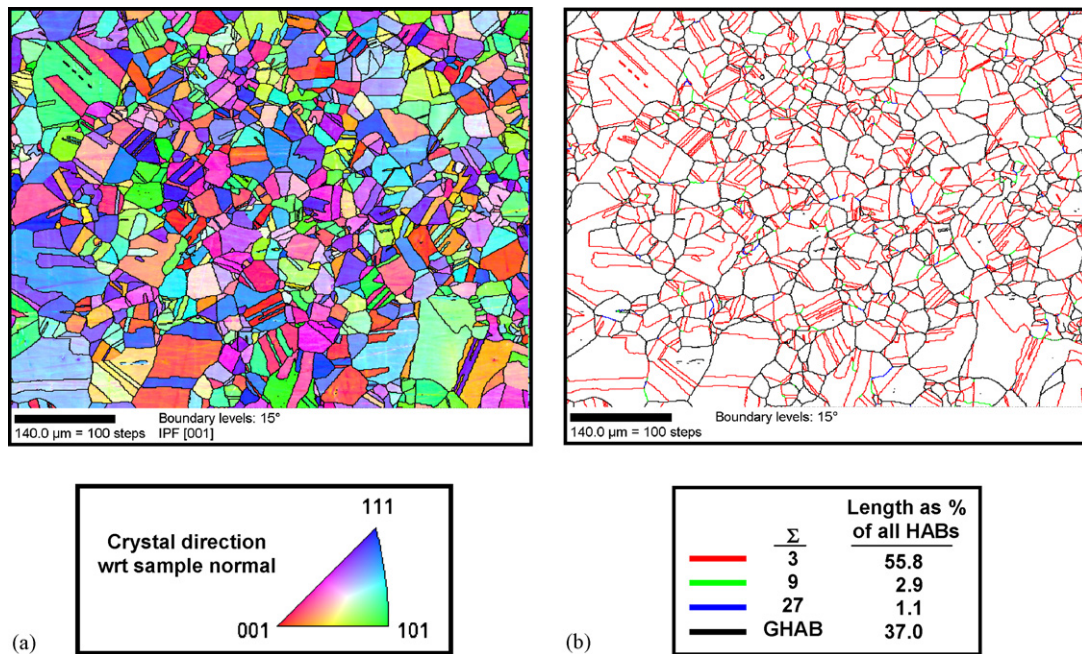


Fig. 5. Grain boundary structure and special boundary populations in AL6XN. (a) Inverse pole figure map of one section, indicating the out-of-plane crystallographic orientation of each grain. (b) Boundary map showing  $\Sigma 3$ ,  $\Sigma 9$ , and  $\Sigma 27$  CSL boundaries, and general high-angle boundaries.

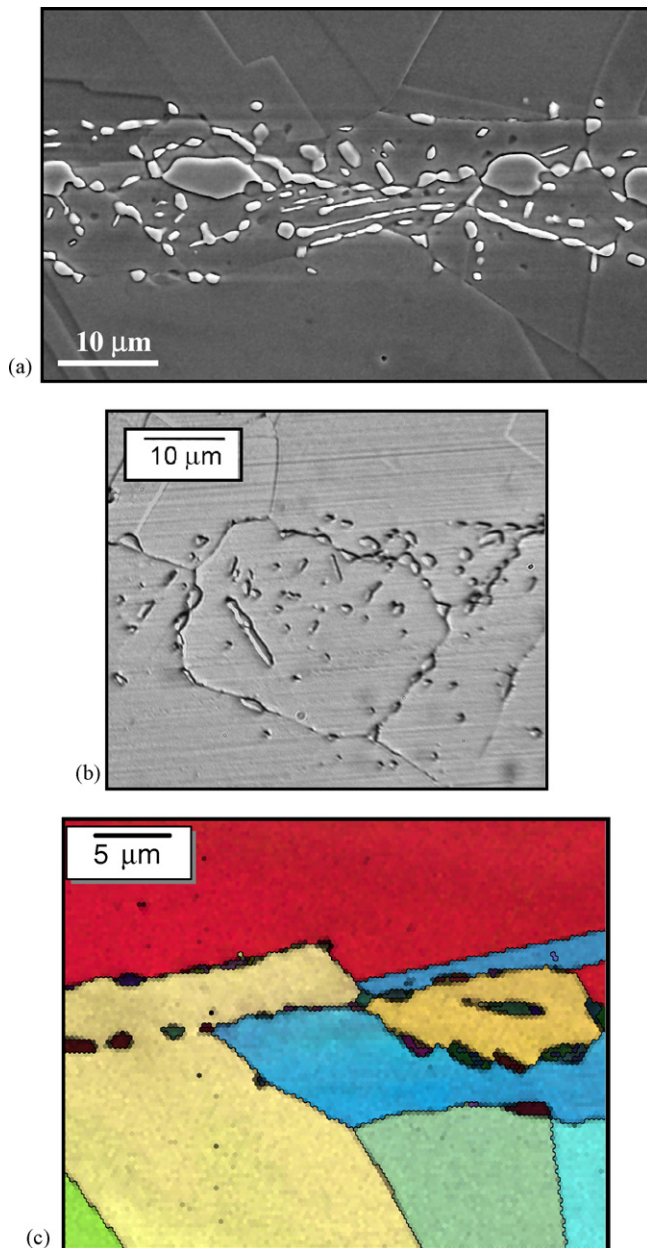


Fig. 6. (a) SEM micrograph showing coarse and fine sigma particles along the centerline of the AL6XN plate. (b) Optical micrograph of sigma particles at austenite grain boundaries and within austenite grains. (c) Orientation map with sigma particles decorating austenite grain boundaries. Color legend is the same as that in Fig. 5(a).

such deleterious effects. In addition, the mechanism by which these particles form should be understood in order to control their evolution, for enhanced material performance. In this regard, TEM imaging, diffraction, and elemental (EDS) analyses have also been performed for determination of the size, morphology, crystallography, and stoichiometry of the precipitate phases in the super-austenitic alloy studied here. One such example is presented in Fig. 7, which contains a bright field TEM micrograph of a sigma precipitate within the austenite matrix (Fig. 7(a)), along with the corresponding selected area diffraction pattern (Fig. 7(b)), and the EDS spectra from the

particle (Fig. 7(c)). These precipitate distributions are also being inputted into the mesoscale image-based finite element models of materials response described in Section 3.3.

Three-dimensional (3D) analyses of both the austenite (matrix) grains and the sigma (precipitate) particles are performed by serial sectioning and 3D reconstructions from optical micrographs, in conjunction with EBSD/OM crystallographic analyses, and also by X-ray tomography. Fig. 8 shows a 3D reconstruction of the austenite matrix grains, with the volume of this reconstruction measuring approximately  $250\text{ }\mu\text{m} \times 250\text{ }\mu\text{m} \times 160\text{ }\mu\text{m}$ . The color legend corresponds to the crystallographic orientation in the direction of the grey arrow indicated in Fig. 8(a) and (b). Combining 3D reconstruction of the microstructure with crystallography is providing a wealth of information about the microstructure that cannot be inferred or calculated from 2D images, in particular the crystallographic normals of grain boundary planes, which are necessary for the full 5 degree-of-freedom definition of the boundary. As mentioned before, these results provide the critical input needed for both the 3D mesoscale image-based models described in Section 3.3, and also to the semi-empirical atomistic models. In the latter case for example, measurements of the grain boundary inclinations directly from 3D reconstructions are used as input conditions for the segregation calculations discussed above. Such grain boundary plane characterization provides far more information regarding the special properties of boundaries than typical misorientation-based descriptions obtained from 2D analyses. Additionally, the 3D distributions of sigma particles (and voids associated with them) are also being obtained by 3D X-ray tomography techniques [34]. These new results are providing important insight into the potential for such sigma (plus void) networks to provide potential fracture paths, and will also be considered in the 3D mesoscale image-based materials models described below.

### 3.3. Mesoscale image-based modeling results

Both 2D and 3D image-based mesoscale finite element modeling (FEM) is performed to simulate stress/strain fields generated in the heterogeneous microstructure, and thus mesoscale stress/strain response of real microstructures under mechanical loading conditions. In these models, 2D and 3D images are used as direct input to generate finite element meshes. A regular grid is created with each pixel (2D) or voxel (3D) at the center of an element in the mesh, and an averaged crystallographic orientation is assigned to each grain. The finite element simulations are conducted using anisotropic elasticity-based constitutive models, and are thus applicable up to the point of initial material yield. The interactions between crystallographic orientation, applied loads, constraints, and microstructural morphology can thus be discerned. Further details of these models are provided in [8,23].

Some representative results from the 2D image-based models are shown in Fig. 9. In this example, regions of maximum and minimum local strains are shown to be a function of the relative grain crystallography, elastic anisotropy, the local grain morphology (e.g., grain corners, etc.), and the externally applied



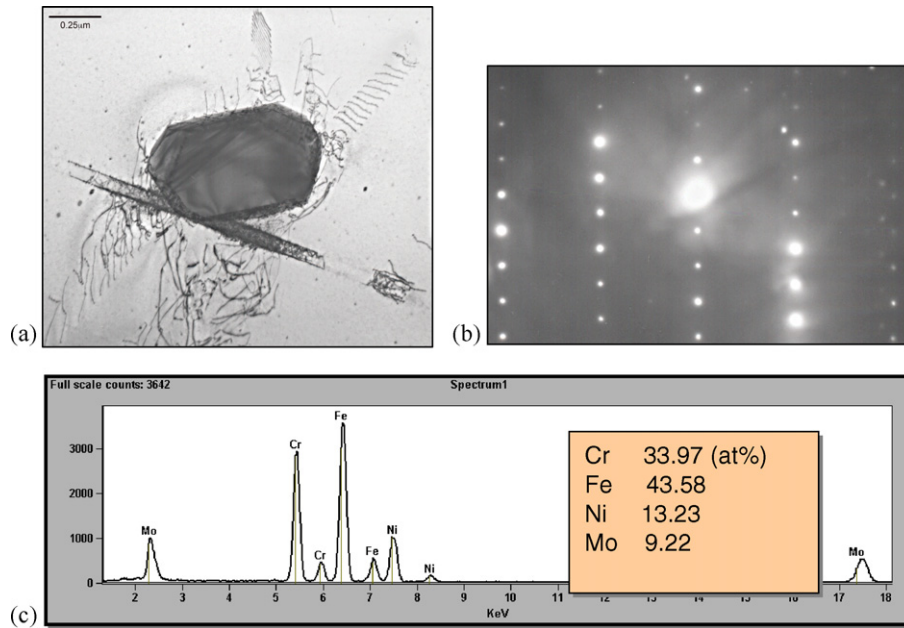


Fig. 7. TEM results of a sigma particle in the austenite matrix. 8(a) bright field TEM image of the sigma particle with dislocations around it; 8(b) corresponding SAD pattern taken with a  $[1\ 1\ 5]_{\sigma}$  beam direction; 8(c) corresponding energy dispersive spectroscopy (EDS) compositional analysis taken from the same particle.

stress state. For instance, these regions are in complex states of local stress or strain, depending on the local grain morphology and crystallography. In the example presented in Fig. 9, the ratio of local strain to applied strain (both normal to the loading direction) ranged from  $-1 < (\varepsilon_{\text{local}}/\varepsilon_{\text{app}}) < 3$ . Therefore, local strain states can be reversed (from positive to negative) in some microstructural regions. These simulations have also shown that such local states of strain (and/or stress) change dramatically depending on the nature of the externally applied stress state, due to elastic anisotropy of each grain and local compatibility requirements. These types of mesoscale models could also be combined with other scaled-up continuum FEM models of stress states generated in various macroscopic components of

Navy ships, such as T-stiffeners in a double hull design, butt joints in deck weldments, etc.

More recently, image based FEM models have been modified at NRL to use real 3D microstructural data as input to simulate more realistic 3D material responses. Besides the differences in the type of experimental data used as input, a major distinction between the 2D and 3D models is the ability to relax the plane strain boundary conditions required in the 2D models. Some initial results are provided in Fig. 10, which shows the contour plots of maximum strain normal to the loading direction resulting from 0.2% applied strain with three different constraint conditions. By comparison with the 2D simulations, even these preliminary 3D simulations have shown

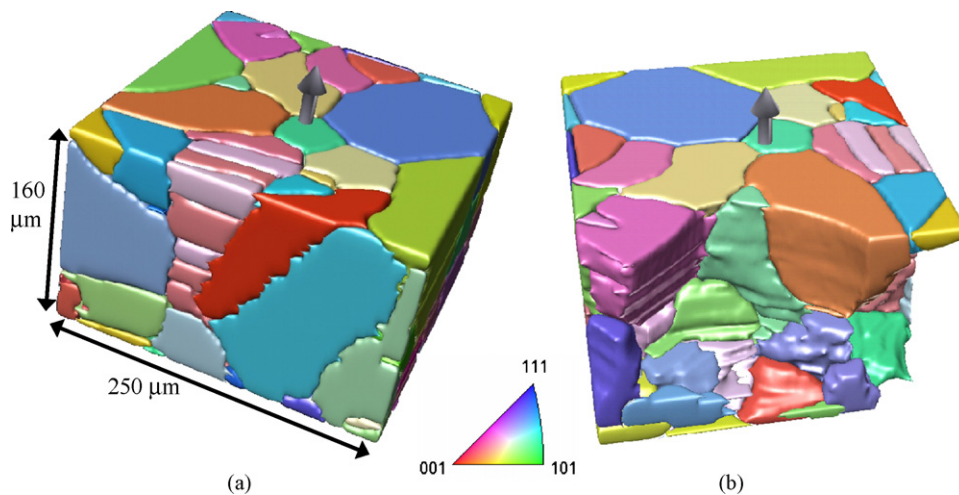


Fig. 8. 3D reconstruction of austenite matrix in AL6XN (taken from [7]). (a) The reconstructed area is approximately  $250\ \mu\text{m} \times 250\ \mu\text{m} \times 160\ \mu\text{m}$ , and contains 138 individual grains and twins. The color key corresponds to the crystallographic direction parallel to the grey arrow, which is also the normal to the sectioning plane. (b) Interior view of the austenite matrix, with some grains removed to show grain morphology.



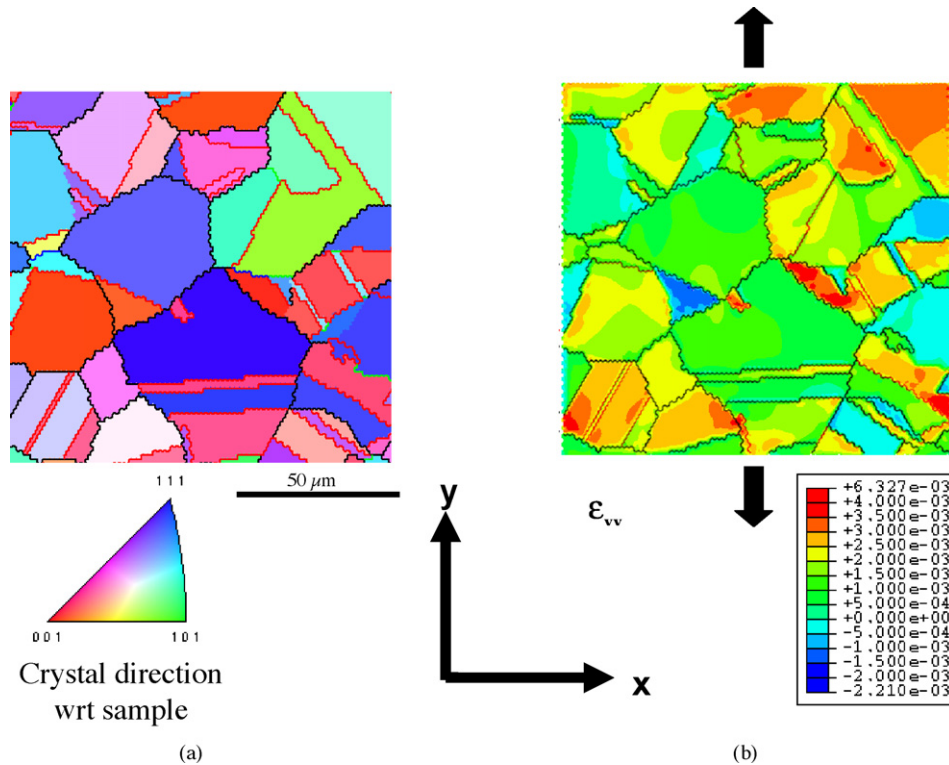


Fig. 9. (a) Example 2D orientation map for austenitic region of super austenitic stainless steel with (b) corresponding image-based model results showing the contour plot of the  $\epsilon_{yy}$  (strain) from uniaxial stretch loading conditions and 0.2% applied strain in the y-direction.

that there are very large differences in the materials response of the microstructure when considered in 3D, as opposed to 2D. That is, the nature, magnitude, and location of the local regions of maximum and minimum stress and strain are very different in 3D, as compared to the results of the 2D calculations of similar microstructures in the same material. For example, high stresses develop around different microstructural features in 2D than in 3D. From 2D image-based FEM simulations, it was

observed that stresses were highest at the regions surrounding grain boundaries, and that different loading conditions resulted in high stresses developing near different types of boundaries. Specifically, for tensile loading conditions, highest stresses were generated near faceted grain boundaries (i.e.  $\Sigma 3$  boundaries), whereas under shear loads, the highest stresses are generated near non-faceted (curved) grain boundaries. A somewhat analogous relationship is observed in three dimensions, however, in

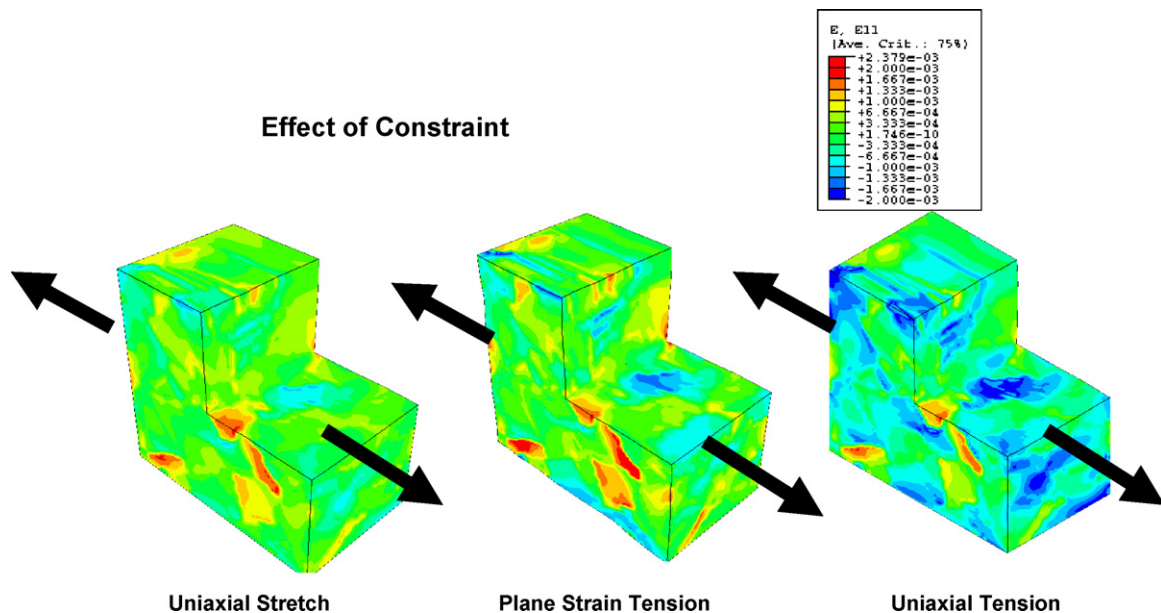


Fig. 10. 3D image-based model results showing contour plots of the strain normal to the loading direction for three different constraint cases.

3D it is the triple junctions (grain edges) where highest stresses are observed under tensile loading conditions. These types of 3D models are thus important for alloy design programs which attempt to accurately predict the mechanical properties of alloys. A more thorough analysis of these results is presented in the more detailed studies [7,8].

#### 4. Summary

This paper provides a brief overview of a multidisciplinary effort at the Naval Research Laboratory (NRL) aimed at developing a methodology to assist in the design of advanced Navy steels. In addition to consideration of some details of the techniques and/or models employed, a few representative results have been presented here. In this way, a description of the types of output produced by this program has been provided, so as to demonstrate how these results are melded across various disciplines and length scales, in order to enhance capabilities for designing advanced Navy steels.

In particular, first principles calculations including density functional theory (DFT), linear augmented plane wave analyses under the generalized gradient approximation (LAPW/GGA), and the Stoner criterion (for magnetic behavior) have been employed in conjunction with atomistic calculations, which rely on a limited amount of experimental data, but can address much larger systems. The latter calculations include the tight-binding method (TBM) to create Hamiltonians which can be extended to systems of thousands of atoms with quantum mechanics, and millions of atoms with semi-empirical angular dependent potentials (ADPs). These potentials, which were developed here for Fe and the Fe–Ni system, include non-central atomic interactions and may later include temperature dependence and magnetic effects. Using the ADP potentials as input, the Monte-Carlo method has been employed to calculate the grain boundary structure, energy, and segregation, and to perform virtual “mechanical testing” of grain boundary decohesion in Fe–Ni alloys representing a prototype of austenite in steels. Examples of output data calculated by these techniques include formation energies of phases, elastic constants, coefficients of thermal expansion, and grain boundary structures, energies and segregation.

Experimental techniques have been applied to a commercial super-austenitic stainless steel (AL6XN) which serves as a baseline composition from which to provide quantitative experimental input, guidance, verification, and enhancements to the models and simulations. The experimental methods include optical microscopy, scanning electron microscopy (SEM), transmission electron microscopy (TEM), energy dispersive spectroscopy (EDS), and electron backscatter diffraction (EBSD) analysis with orientation mapping (OM), as well as serial sectioning and X-ray tomography in conjunction with computer-based three-dimensional (3D) reconstruction, scientific visualization, and quantitative analyses. Data thus obtained include grain and grain boundary statistics based on both misorientation and 3D boundary plane analysis (e.g., frequency of special grain boundaries, grain boundary inclinations in 3D, etc.), compositional analyses of precipitates and matrix grains, and three-dimensional morphology, interconnectivity,

and crystallography of matrix and precipitate grains. These results provide critical guidance to the lower-scale first principles and atomistic models, and are the direct input required for image-based mesoscale FEM models of materials response.

The image-based mesoscale models are applied to 2D images/micrographs, as well as to 3D reconstructions taken from real (experimentally obtained) microstructures, and use finite element techniques to simulate stress and strain evolution at the mesoscale. These 2D and 3D models take the real microstructure (inputted into the FEM mesh), apply various stress states, and allow the stress and strain to evolve within the microstructure. In this way, these models examine the interactions between grain morphologies, elastic anisotropy, and applied stress states. Particular emphasis is placed on the identification of microstructural regions that develop high local stresses and strains which will initiate plasticity and may eventually lead to failure. Additionally, novel stress/strain visualization techniques have been developed for the mesoscale modeling results; these techniques provide for a better understanding of how the heterogeneous deformation fields, due to microstructure, produce mechanical response at the mesoscale.

In all components of this multidisciplinary program, data is passed (in both directions) between team members and across various length scales, and the results are being integrated in such a way as to be able to provide guidance for prediction and design of optimized alloy compositions and processing procedures. Only a few representative results from each of the tasks have been presented here, in order to provide a brief overview of the program. More thorough analyses from each of the components of this effort are provided in a number of companion papers to this one [5–8]. Additionally, ongoing efforts are centered about further application of this methodology to alloy design. For example, using the methods described here, changes in alloy composition (in this case changes in Ni, Cr, and C about the AL6XN baseline composition) are being examined for their simultaneous effects on the magnetic properties, phase stability, and potential precipitation reactions. Additionally, the distributions of grain boundary types (e.g.,  $\Sigma 3$ ,  $\Sigma 9$ , and general grain boundaries) and their effect on the overall mechanical (through FEM models) and corrosion response are being investigated. Variations in thermal processing cycles can also be considered in a similar fashion. The ultimate goal of such examinations is to provide recommendations for optimum composition ranges and processing cycles with respect to magnetic, corrosion, and mechanical properties.

#### Acknowledgments

The authors from NRL and George Mason University gratefully acknowledge funding of this project by the Office of Naval Research (Grant # N0001404WX20553, Dr. Julie Christodoulou, program manager), while the work of JFB was performed under the auspices of the U.S. Department of Energy under Contract W-7405-Eng-36. The authors also wish to acknowledge the significant efforts of Mr. Leroy Levenberry in performing the serial sectioning for the 3D reconstructions.

## References

- [1] G.B. Olson, *Science* 277 (1997) 1237.
- [2] G.B. Olson, *Science* 288 (2000) 993.
- [3] T. Shishidou, J.H. Lee, Y.J. Zhao, A.J. Freeman, G.B. Olson, *J. Appl. Phys.* 93 (10) (2003) 6876–6878.
- [4] L. Vitos, A.P.A. Korzhavyi, B. Johansson, *Mater. Today* (2002) 14–23 (October issue).
- [5] M.J. Mehl, D.A. Papaconstantopoulos, I.I. Mazin, N.C. Bacalis, W.E. Pickett, *J. Appl. Phys.* 89 (2001) 6880;  
M.J. Mehl, D.A. Papaconstantopoulos, in: S. Yip (Ed.), *Handbook of Materials Modeling*, Springer, The Netherlands, 2005, pp. 275–305.
- [6] Y. Mishin, M.J. Mehl, D.A. Papaconstantopoulos, *Acta Mater.* 53 (2005) 4029–4041.
- [7] A.C. Lewis, J.F. Bingert, D.J. Rowenhorst, A. Gupta, A.B. Geltmacher, G. Spanos, *Mater. Sci. Eng. A* 418 (2006) 11–18.
- [8] A.C. Lewis, A.B. Geltmacher, *Scripta Mater.* 55 (2006) 81–85.
- [9] P. Hohenberg, W. Kohn, *Phys. Rev.* 136 (1964) B864;  
W. Kohn, L.J. Sham, *Phys. Rev.* 140 (1965) A1133.
- [10] O.K. Andersen, *Phys. Rev. B* 12 (1975) 3060;  
S.H. Wei, H. Krakauer, *Phys. Rev. Lett.* 55 (1985) 1200.
- [11] J.P. Perdew, J.A. Chevary, S.H. Vosko, K.A. Jackson, M.R. Pederson, D.J. Singh, C. Fiolhais, *Phys. Rev. B* 46 (1992) 6671.
- [12] M.M. Sigalas, D.A. Papaconstantopoulos, *Phys. Rev. B* 50 (1994) 7255.
- [13] R.E. Cohen, M.J. Mehl, D.A. Papaconstantopoulos, *Phys. Rev. B* 50 (1994) 14694;  
M.J. Mehl, D.A. Papaconstantopoulos, *Phys. Rev. B* 54 (1996) 4519;  
D.A. Papaconstantopoulos, M.J. Mehl, *J. Phys.: Condensed Matter* 15 (2003) R413.
- [14] X. Xie, Y. Mishin, *Acta Mater.* 50 (2002) 4303–4313.
- [15] M.A. Mangan, G.J. Shiflet, in: W.C. Johnson, J.M. Howe, D.E. Laughlin, W.A. Soffa (Eds.), *Proceedings of the International Conference on Solid–Solid Phase Transformations*, TMS, Warrendale, PA, 1994, pp. 547–552.
- [16] T.L. Wolfson, W.H. Bender, P.W. Voorhees, *Acta Mater.* 45 (6) (1997) 2279.
- [17] M.V. Kral, G. Spanos, *Acta Mater.* 47 (1999) 711–724.
- [18] A. Tewari, A.M. Gohkale, *Mater. Characterization* 44 (2000) 259–269.
- [19] K.M. Wu, M. Enomoto, *Scripta Mater.* 46 (2002) 569–574.
- [20] R.E. Hackenberg, D.P. Norstrom, G.J. Shiflet, *Scripta Mater.* 47 (2002) 356–361.
- [21] J.E. Spowart, H.M. Mullens, B.T. Puchala, *J.O.M.* 55 (10) (2003).
- [22] M.V. Kral, G. Spanos, *Metall. Mater. Trans. A* 36 (2005) 1199–1207.
- [23] A.B. Geltmacher, K.E. Simmonds, in: A.S. Khan, O. Lopez-Pamies (Eds.), *Plasticity, Damage, and Fracture at Macro, Micro, and Nano Scales*, Neat Press, 2002, pp. 699–701.
- [24] H. Chamati, N.I. Papanicolaou, Y. Mishin, D.A. Papaconstantopoulos, *Surf. Sci.*, submitted for publication.
- [25] P. Lejcek, S. Hofmann, V. Paidar, *Acta Mater.* 51 (2003) 3951–3963.
- [26] K.T. Aust, U. Erb, G. Palumbo, *Mater. Sci. Eng. A* 176 (1994) 329–334.
- [27] P. Peralta, L. Llanes, J. Bassani, C. Laird, *Phil. Mag. A* 70 (1994) 219–232.
- [28] D.C. Crawford, G.S. Was, *Metall. Trans. A* 23 (1992) 1195–1206.
- [29] J. Don, S. Majumdar, *Acta Metall.* 34 (1986) 961–967.
- [30] J.Q. Su, M. Demura, T. Hirano, *Acta Mater.* 51 (2003) 2505–2515.
- [31] B.W. Bennett, H.W. Pickering, *Metall. Trans. A* 18 (1987) 1117–1124.
- [32] H.Y. Bi, et al., *Scripta Mater.* 49 (2003) 219–223.
- [33] E.A. Trillo, L.E. MurrLE, *Acta Mater.* 47 (1998) 235–245.
- [34] R.W. Fonda, E. Lauridsen, W. Ludwig, P. Taffereau, G. Spanos, *Scripta Mater.*, submitted for publication.